Modern Physics Letters A
Vol. 30, No. 17 (2015) 1540024 (14 pages)

DOI: 10.1142/S0217732315400246

Proton computed tomography

Martina Bucciantonio*,† and Fabio Sauli*,‡

*Tera Foundation, via Puccini 11, 28100, Novara, Italy
†Albert Einstein Center for Fundamental Physics (AEC), Laboratory for High Energy Physics (LHEP), University of Bern, Sidlerstrasse 5, CH-3012 Bern, Switzerland
‡CERN, CH-1211 Geneva 23, Switzerland
†martina.bucciantonio@cern.ch
‡fabio.sauli@cern.ch

Received 15 January 2015
Accepted 20 February 2015
Published 5 May 2015

Proton computed tomography (pCT) is a diagnostic method capable of *in situ* imaging the three-dimensional density distribution in a patient before irradiation with charged particle beams. Proposed long time ago, this technology has been developed by several groups, and may become an essential tool for advanced quality assessment in hadrontherapy. We describe the basic principles of the method, its performance and limitations as well as provide a summary of experimental systems and of results achieved.

Keywords: Proton tomography; range; hadrontherapy.

1. Introduction

The advantages of using intense charged particle beams for deep tumor therapy have been explored since the early operation of accelerators built for particle physics experimentation. Pioneering works with proton beams took place in the early '50s in Berkeley;[1] further studies in other laboratories extended the method to the use of light ions, opening a wide field generally called today hadrontherapy.

In the ensuing years, these early developments led to the worldwide construction of many accelerators dedicated to medical applications with a recent estimate of around 120,000 patients treated with charged particle beams.[2–5] Treatment quality assurance methods under development exploit the detection of the secondary yields, prompt gammas or charged particles, emitted during the irradiation; ENVISION, a ground-breaking European FP7 project, established the basis for the implementation of several patient monitoring techniques.[6] Nevertheless, no standard tools exist to actively monitor the patient during the exposure.

The possibility of obtaining in-beam radiographic images of a patient recording the two-dimensional (2D) maps of the energy loss of the beam itself was discussed

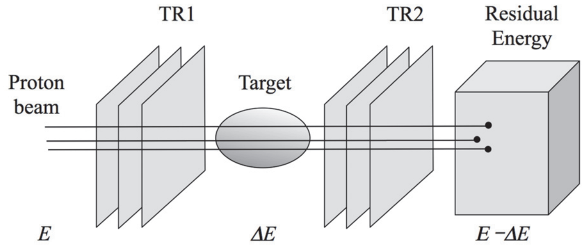

Fig. 1. Schematics of a proton radiography system for a homogeneous target.

in the late '60s.[7] Further studies demonstrated the effectiveness of the method for the measurement of the integrated electron density distribution in a phantom; with several exposures at different angles, the tomographic image can then be obtained using the reconstruction methods described in Sec. 4.

A scheme of a proton radiography setup is illustrated in Fig. 1. Proton computed tomography (pCT) is obtained by means of several projections at different angles. The object under investigation (hereby named "target") is exposed to a beam of energy E exceeding the total absorption. Position and direction of the particles are measured in a set of position-sensitive trackers before (TR1) and after (TR2) the target; the energy loss in the target, ΔE, is deduced from the measurement of the proton residual energy or range with an appropriate detector. The average target density projected on a plane perpendicular to the beam is then inferred from the position-dependent correlation between position and energy loss, either on a track per track basis, or averaged over a range of positions.

The energy loss in the target depends on its thickness and average density. According to NIST PSTAR database, the range in tissue equivalent plastic (A150) for 200 MeV protons is 25.8 cm, which is sufficient to penetrate an adult human skull (nominal width of 20 cm in anterior–posterior direction).[8] For 250 MeV protons, the range in A150 is 33.7 cm, sufficient to penetrate an adult trunk (nominal width of 34 cm, excluding arms).

The precision in the determination of the average target density depends on several factors: statistical errors (number of recorded particles per pixel), energy loss straggling, beam and instrumental dispersions. As an example, Fig. 2 shows a comparison between computed and measured density resolutions for a water phantom and a 215 MeV proton beam,[9] as a function of the number of recorded particles per pixel. The pCT image quality is determined, aside from the localization accuracy of the tracking devices, by the dispersive effect of multiple Coulomb scattering (MCS) of the particles in the target, as it will be discussed in Sec. 3. Because of detector limitations, and to minimize the dose absorbed by the patient, the exposure is usually done at beam intensities three or four orders of magnitude lower than those used for therapy; to be exploitable, a meaningful image should be recorded within a fraction of a minute, imposing strict requirements to the rate capability of the system.

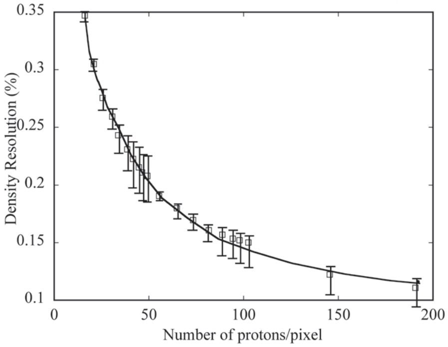

Fig. 2. Computed (full line) and measured density resolution for a water target as a function of the number of particles per pixel. © 1995 AAPM. Reprinted, with permission, from Ref. 9.

The peculiar feature of the pCT method, compared to a standard X-ray computerized tomography (xCT), is that it can be performed in-beam, permitting to verify the position of the organs to be irradiated immediately prior to the patient exposure and, if needed, to accordingly modify the treatment plan.

After a reminder of the major characteristics of the interaction processes of protons in matter, this note describes the development, performance and limitations of imaging systems based on the measurement of the residual energy of the particles emerging from the target.

2. Energy Loss of Protons in Matter

Charged particles gradually lose their energy in matter through electromagnetic and nuclear interactions. Figure 3(a) shows the differential energy loss, or stopping power, and the range of protons in water in the energy interval of interest for hadrontherapy.[8] The energy loss per unit length of material increases with the

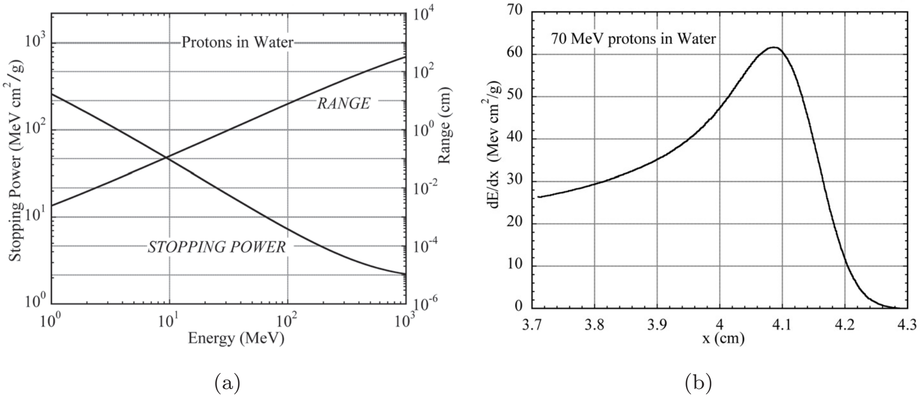

(a) (b)

Fig. 3. (a) Stopping power as a function of proton energy in water. (b) End-of range differential energy loss as a function of penetration for protons in water.

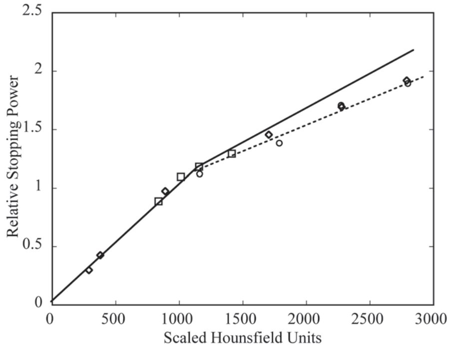

Fig. 4. Computed (solid line and diamonds) and measured (dashed line and squares) correlation between the HU for a range of biological materials and the proton relative stopping power. © 1995 AAPM. Reprinted, with permission, from Ref. 9.

decrease of the particle energy. When the proton approaches the end of range, the differential energy loss plotted as a function of thickness has a characteristic shape, the Bragg peak, as shown by the example in Fig. 3(b), computed for a water phantom.[10] This is the feature exploited in hadrontherapy to target the region of the lesion sparing the surrounding tissues, and has also as consequence that a measurement of the penetration depth in a range detector provides a rather accurate estimate of the residual energy. Additionally, pCT can, in principle, achieve the image quality of xCT with lower doses to the patient.

The incremental energy loss of a proton in a material is the integral on the differential energy loss over the track length L. For a non-homogeneous material, this can be written as:

$$\Delta E = \int_0^L \left(\frac{dE}{dl}\right)_l dl = \int_0^L \rho(l) S(l, E_l) dl \,, \tag{1}$$

where $\rho(l)$ is the electron density and $S(l, E_l)$ the stopping power on the medium at depth l and residual energy E_l. A measurement of the energy loss over a given material thickness provides therefore the density distribution in the target.

The penetration depth depends on the beam energy as well as on the incremental energy loss along the path, itself a function of the electron density of the tissues traversed; a precise knowledge of the position-dependent density distribution in the target is therefore paramount for the design of the treatment plans. This goal is achieved using standard xCT scans of the patient, sensitive to the density and atomic number of the constituents; the measured Hounsfield units (HU), which are an expression of electron densities, have to be converted to proton stopping powers for proton therapy, through suitable calibration curves. The process is intrinsically subject to errors, reflecting in inaccuracies of the treatment plan; one objective of a direct density measurement through proton beam tomography is to reduce these errors, as well as to confirm the position of the patient with respect to the beam. A comparison of computed and measured values of the HU for materials of biological relevance is given in Refs. 9 and 11 and Fig. 4 gives an example of correlation between the HU and the proton stopping power, normalized to water. Relative stopping powers for a range of tissue-equivalent materials have been measured and compared to the predictions obtained with xCT in Refs. 12 and 13.

3. Range Straggling and Multiple Coulomb Scattering

On their path through the target, protons lose energy and experience MCS resulting in deviations from a straight line. The statistics of energy loss in the collisions (straggling) affects the residual energy determination, while the spatial resolution of the images is limited by the lateral deflections and scattering angle of the particles in the target. In first approximation and for thin homogeneous materials, the distributions of the scattering angle θ and of the lateral displacement y are quasi-Gaussian, with standard deviations given by:

$$\sigma_\theta = K\sqrt{\frac{x}{X_0}} \quad \text{and} \quad \sigma_y = \frac{1}{\sqrt{3}} x\sigma_\theta\,, \tag{2}$$

where x and X_0 are the material thickness and radiation length and K is a constant. For statistical reasons, the two quantities are correlated, a large deflection angle corresponding to large lateral displacements. More rigorous values for thick materials, together with the distributions for composite materials, are provided by Monte Carlo calculations, taking into account the energy loss along the trajectory.[14]

A measurement of the particle trajectory before and after the target allows to select tracks that have experienced a small deflection, thus improving the image quality at the expense of a reduced tracking efficiency. A more detailed discussion about the effects of straggling and multiple scattering on resolution can be found in Refs. 14–16.

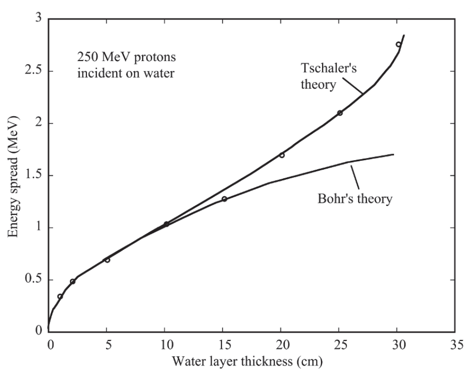

(a)

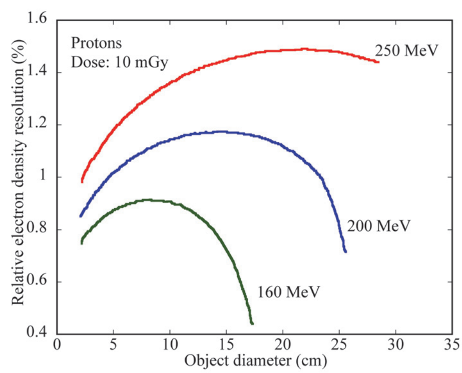

(b)

Fig. 5. (a) Energy straggling for 250 MeV protons in water, computed with GEANT4 (full points) and with two theoretical models. (b) Resolution in a cylindrical water phantom as a function of diameter and proton energy. © 2005 IEEE. Reprinted, with permission, from Ref. 16.

Figure 5(a) shows the standard deviation of the energy loss as a function of water thickness for 250 MeV protons, computed with the GEANT4 simulation program (full points) and with the prediction of two theoretical models.[16] For a 10 cm target, the statistical energy straggling is 1 MeV rms (or 0.4%), to which one should add the resolution of the residual energy measurement in a pCT instrument.

Figure 5(b) shows the relative electron density resolution as a function of the diameter of a cylindrical water phantom impiged with several proton beam energies and a dose of 10 mGy. For each energy, the resolution is worsened by straggling until reaching a plateau; near the end of range, the resolution improves due to the increased stopping power near the end of the Bragg peak.

The energy resolution improves, as expected, as the square root of the dose for a given target, as shown in Fig. 6(a) for different beam energies, reaching the 1% level above 10 mGy, an acceptable dose for medical diagnostics.[16]

The considerations above help to determine, for a given target size and average density, the beam energy needed for optimum resolution. For non-uniform objects, a process named range dilution adds to the dispersions. A proton passing near the interface between a high and a low density material in the target can take either path, depending on the value of the MCS angles; protons with the same incoming direction take different paths and broaden the range spectrum. The process can be exploited to enhance the image in the transition regions.[17] To avoid artifacts around the target-air interface, it is common practice, whenever possible, to plunge the object in a water bath.

For proton energies above ~ 50 MeV, the contribution of inelastic nuclear interactions becomes non-negligible, resulting in the creation of secondary particles or isotopes of the constituents; those processes can be exploited for alternative quality assurance methods. Figure 6(b) shows the fraction of events out of a 16.2 cm

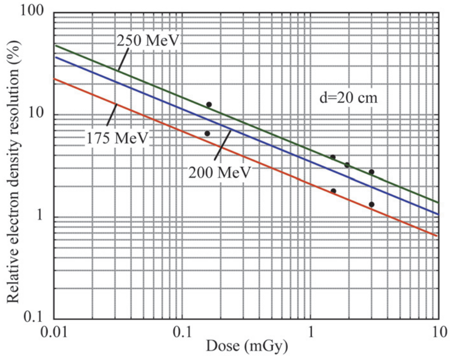

(a)

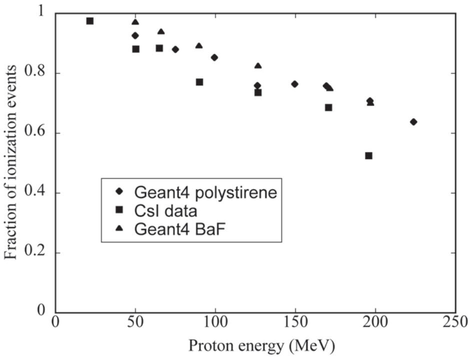

(b)

Fig. 6. (a) Relative density resolution computed as a function of dose for a 20 cm diameter water phantom. © 2005 IEEE. Reprinted, with permission, from Ref. 16. Full dots are experimental values. (b) Fraction of events not affected by inelastic interactions as a function of proton energy, computed with different models. © 2011 IEEE. Reprinted, with permission, from Ref. 18.

polystyrene phantom not affected by inelastic collisions, as a function of proton energy, computed with different models;[18] the fluence is reduced by 30% at 200 MeV, affecting the efficiency of the pCT and increasing the imparted dose.

4. Image Reconstruction Methods

A proper pCT reconstruction algorithm has to build up the relative electron density image of the target, computed on a track per track basis, taking into account the proton angular dispersions. Density and spatial resolutions are the main metrics to evaluate the image quality.

The density resolution is estimated by the contrast to noise ratio between two adjacent regions of different densities.

The spatial resolution is defined as the minimum size, in millimeters, needed to identify a region of interest. It can be quantified with a 2D modulation transfer function (MTF). The MTF is a measure of the signal transmission properties of the imaging system as a function of spatial frequency. For this measurement, the point spread function of details of the image is used. Following the reconstruction, a 2D fast Fourier transform of the region of interest centered on the point spread function is carried out.[19] The characterization of the MTF and studies on spatial resolution in the case of proton/carbon radiography using Monte Carlo simulations have been performed on patient-like phantoms, modeled with cube-shaped inserts composed by different densities of bone and lung, exposed to different proton energy beams.[20]

The pCT image reconstruction commonly makes use, as starting point, of already implemented fast and robust xCT techniques like the filtered back projection (FBP).[21] Several iterative procedures and reconstruction methods have been developed to cope with the degraded spatial resolution due to MCS and to optimize the image processing procedure.

The FBP allows deducing the attenuation coefficient map of an object from a set of measurements of the X-ray absorption along several directions. It is based on the inversion of the Radon transform, the mathematical operator that describes the process of parallel projections, assuming that particles traverse the medium along several directions in a straight line path (SLP). For pCT, the electronic density map with respect to a reference medium (e.g. water) is derived by the Eq. (1) using as input data the incoming and outcoming proton energy in various directions inside the target. Other forms of the FBP algorithm, like the Feldkamp–Davis–Kress,[22] are commonly implemented nowadays and make use of the assumption that each proton path through the object is a straight line and follows a cone-beam geometry. Proton CT images reconstructed with FBP based methods exhibit poor spatial resolution due to MCS that makes the straight line approximation inaccurate, but, on the other hand, good density contrast (low noise) in comparison to xCT. Several Monte Carlo studies proved that FBP is able to produce images in very short time with sufficient resolution for a first assessment of the target during the patient positioning verification procedures before treatment (e.g. see Ref. 23). FBP performances were

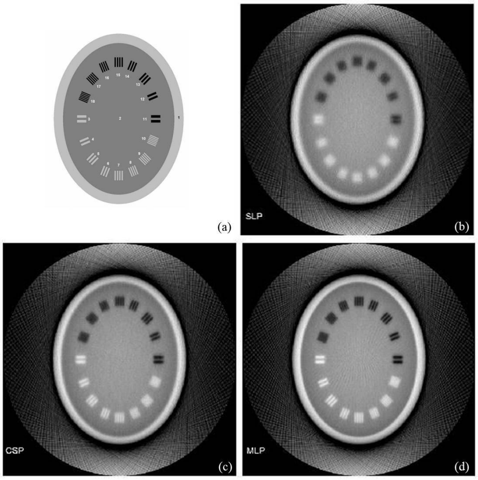

Fig. 7. Reconstruction of the (a) phantom, using (b) the SLP estimator, (c) the cubic spline path (CSP) and (d) the MLP. © 2006 AAPM. Reprinted, with permission, from Ref. 25.

evaluated also on real data by imaging a cylindrical PMMA phantom with a proton beam.[24]

Better spatial resolution can be achieved when a path of maximum likelihood that takes MCS into account is used,[14] instead of the straight-line assumption. Proton direction and location before and after the phantom are the inputs for finding the particle most likely path (MLP). Figure 7, from Ref. 25, shows the simulation study results of a phantom used to test different reconstruction methods. The line pairs are composed of either bone (white) or air (black), placed in a water tank surrounded by a bone shell. The simplest solution of the straight proton path through any media is compared with two estimator of the proton path length: the MLP and the CSP approaches, both of them applied using algebraic reconstruction technique. The straight path assumption provides the worst estimate of the pCT prediction, where a resolution of 2.5 line paires per cm (lp/cm) was observed. The two proton path estimators show superior spatial resolution, 5 lp/cm in the MLP and 4.5 lp/cm in CSP. The algebraic reconstruction technique,[26] an iterative projection method for solving a system of equations, has been found to handle well the nonlinear paths but requires computer intensive procedures.

Inherently parallel block-iterative or string-averaging iterative projection methods executed on multiple processors simultaneously have been proposed as the next step towards the optimization of both spatial and density resolution of pCT images,[23] taking advantage of an initial FBP-reconstructed image estimate. The analysis of the image quality, when reconstructing simulated pCT data with iterative techniques, has demonstrated that both spatial resolution and mean reconstructed relative stopping power values improve with an increasing number of iterations. However, due to inconstancies in the measured data arising from proton energy

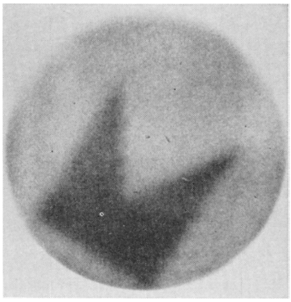

(a)

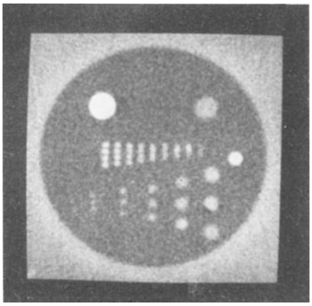

(b)

Fig. 8. (a) Proton absorption radiography of a composite aluminum mask, 7 cm in diameter, recorded on a photographic plate. © 1968 AAAS. Reprinted, with permission, from Ref. 7. (b) PCT for a 19.3 cm diameter polyethylene phantom with holes between 12.7 and 3.2 mm. © 1981 Institute of Physics and Engineering in Medice. Reproduced by permission of IOP Publishing from Ref. 28. All rights reserved.

straggling and MCS, the noise in the reconstructed image can increase with successive iterations. A total variation superimposition method has been proposed to be applied with block iterative projections to enhance the image quality,[19] in particular in term of noise reduction and superior density resolution.

A scattering radiography, where a density level of each pixel is associated to the mean value of the proton scattering angle, provides information about the proton scattering power of materials, which is inversely proportional to the effective atomic number distribution in the tissue. Energy loss radiography cannot provide this information since stopping power depends only on the ratio atomic number and mass which is practically identical for most soft tissues and water, leading to very low contrast. Therefore, scattering radiography, although the image has lower quality than the energy loss radiography, will likely have useful applications in proton treatment planning.

For the time being most commercial proton accelerators provide beams with a maximum energy around 230 MeV, corresponding to a range of 33 cm in water. In some cases, this is not enough for the full angular coverage of the tomographic reconstruction, leading to severe artifacts in the projected images. Simulation studies have been carried out combining the prior knowledge of xCT of a commercial phantom with simulated proton data, as in Ref. 27. In the case of limited angles, dual modality reconstruction yields the high spatial resolution of the xCT while maintaining the improved stopping power estimation of pCT.

5. Experimental Setups and Measurements

One of the earliest examples of proton radiography is shown in Fig. 8(a),[7] recorded on a wide proton beam with a photographic emulsion after traversing a thick composite aluminum mask designed to have an additional pennant-shaped foil, 130 μm thick, at the edge of full absorption. As noted by the author, the method has good density resolution, but poor space resolution, due to multiple scattering of the protons at the end of range. With a setup consisting of a position-sensitive detector, a multiwire proportional chamber (MWPC) with delay line readout, followed by a high-purity Germanium crystal to measure the residual energy, the authors of Ref. 28 recorded the image of a circular polyethylene phantom with holes of different diameter, exposed to a narrow 240 MeV proton beam (see Fig. 8(b)). In the setup, both the beam and the detector were fixed in position, while the phantom, immersed in a water bath to provide a near constant absorption thickness, was moved in steps to realize a scan of the object; a filtered back-projection algorithm was used for the image reconstruction. The authors achieved a density resolution of 1.8% with a position resolution of ~ 1 mm in both coordinates.

The mechanical target scanning method, appropriate for preliminary studies, does not meet the criteria for a diagnostic use. The development of a system capable of performing proton radiography and tomography started in the mid-90s at the Paul Scherrer Institut (PSI) in Switzerland, in the framework of their proton therapy program. Making use of a pair of medium-size MWPCs to record the particle coordinates and a NaI crystal, 7.5 mm in diameter, for the measurement of the residual energy, the setup was used both to realize preliminary pCT images of anatomic phantoms and to measure the HU for a range of biological materials (see Ref. 9).

To overcome the rate limitations of the MWPC-based system, the PSI detector was later rebuilt using two scintillating fiber hodoscopes, with an acceptance area of 220×32 mm^2 and 1 mm spatial resolution; the measurement of energy was replaced by the intrinsically faster recording of the residual range in a stack of 64 scintillating plastic tiles, individually readout by pairs of wavelength shifting fibers coupled to photomultipliers, decreasing costs and improving the response uniformity than in the case of scintillation crystals (see Ref. 29). In the same work, the combined uncertainty, σ_R, in the range R resulting from the dispersion due to straggling, σ_s, and to the momentum spread of the beam, σ_p, can be written as:

$$\sigma_R = R\sqrt{\left(\frac{\sigma_s}{R}\right)^2 + \left(\frac{\sigma_p}{R}\right)^2}\,. \tag{3}$$

Despite its discrete conception, the range telescope provides a resolution better than the thickness of the tiles when averaging on a number of protons; the uncertainty on the mean value of R is then $\sigma_R/\sqrt{N}$ where N is the number of tracks recorded on a given image pixel. Assuming the residual range to be proportional to the integrated density over a target of length L, the corresponding density resolution is then:

$$\frac{\sigma_\rho}{\rho} = \frac{\sigma_R}{L\sqrt{N}}\,. \tag{4}$$

For the conditions of their system, and with a 177 MeV proton beam (213 mm average range in water), the authors estimated a density resolution of 0.3% for a water target 15 cm thick and 200 protons per pixel.

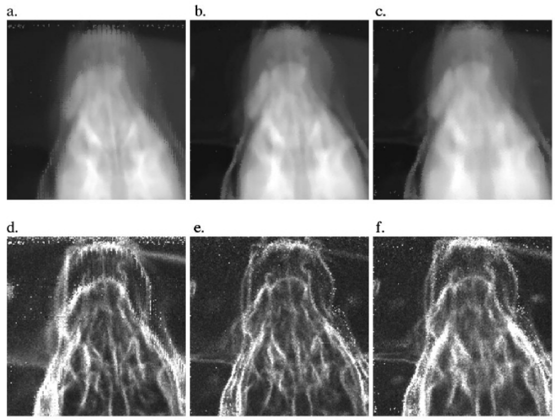

Fig. 9. Dog's head pCT images reconstructed at different depths (top row) and corresponding range dilution images (bottom row). © 2004 AAPM. Reprinted, with permission, from Ref. 17.

(a)

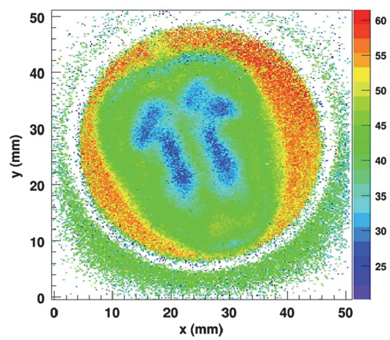

(b)

Fig. 10. (a) pCT of a hand phantom. © 2014 IEEE. Reprinted, with permission, from Ref. 32. (b) Proton radiography of a walnut at 62 MeV. © 2011 Elsevier. Reprinted, with permission, from Ref. 37. All rights reserved.

Figure 9 shows proton radiographies of a dog's head, recorded at PSI with the described instrument,[17] by scanning the proton pencil beam (10 mm FWHM) in one direction and moving the patient table along the other direction perpendicular to the beam. Limited by the acquisition time and for $\sim 10^7$ recorded proton, a radiography could be recorded in about 20 s.

Started in the early 2000s,[30] a collaboration of several groups mostly based in California has developed pCT systems,[31] numerous related image analysis methods and reconstruction algorithms, as mentioned in the previous sections. In its most recent design, the system has two pairs of X–Y silicon microstrip detectors for tracking the protons before and after the target, and a matrix of 18 CsI:Tl crystals,

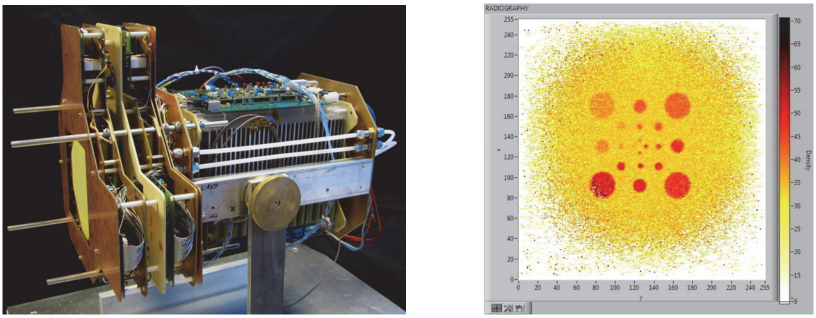

(a) (b)

Fig. 11. (a) The TERA PRR10 system, showing the two GEM detectors and the 30 scintillators stack. (b) 100 MeV proton radiography of a Plexiglas plate with a pattern of holes. The smallest holes are 1 mm in diameter.

12.5 cm long each, to measure the residual energy. An example of pCT radiography of a hand phantom,[32] recorded with the Loma Linda 200 MeV proton beam is shown in Fig. 10(a), plotted with 0.5 mm resolution pixels; the image shows well a major feature of proton radiography, as compared to xCT, the relatively small difference of contrast between tissue and bone which differ by 50–80% in density respect to water. In the same work, the authors compare the results of the conventional energy loss radiography and the scattering radiography.

The Italian collaboration PRIMA is developing a device similar in conception,[33] made by 50×50 mm^2 silicon microstrip trackers and inorganic crystal scintillators as calorimeter. Use of fast scintillators, Cerium-doped YAP or YAG crystals,[34] allows to overcome the rate limitations encountered in the previously described system. The detector aims to reach data acquisition rates close to one MHz.[35] Preliminary measurements were performed exposing the detector to a 200 MeV proton beam at Loma Linda,[36] and to 62 MeV proton beam of the INFN-LNS laboratory[37] (see a walnut radiography in Fig. 10(b)).

A research program of the TERA foundation started in 2009 with the aim of building a proton radiography system similar in design to the PSI device, replacing the fibers tracker with position-sensitive gaseous detectors, followed by stacks of organic plastic scintillator slabs. Use of gas electron multiplier (GEM)[39] for tracking has several advantages as compared to the other systems: very high intrinsic rate capability (well above 1 MHz cm^2), light construction in the active area (below 1% of a radiation length), good localization accuracy (~ 100 μm) and large detection areas.[40] The first prototype, named PRR10,[38] has an acceptance of 10×10 cm^2, the calomireter is segmented in 30 scintillators of 3 mm in thickness, readout by wavelength fibers coupled to silicon photomultiplier sensors. Figure 11(a) shows the PRR10 detector exposing the various components. For each event, the x–y coordinates of the protons are recorded in the two GEM chambers, as well as the signal amplitude in each scintillator. The residual range is then obtained detecting the last scintillator with a signal above noise; the accuracy in the range determination is better than the scintillator thickness, since for a monoenergetic beam the various dispersions add up spreading the end of range over several counters. Figure 11(b) shows the proton radiography, taken at PSI with protons at 99.7 MeV,[41] of 20 mm Plexiglas plate target with holes different in diameter and depth; the smallest holes (1 mm in diameter) are well resolved. From the recorded contrast, one can infer an intrinsic range resolution of 1.7 mm corresponding to a density resolution of 0.11% when traversing 15 cm of water equivalent. Due limitations of the electronics, the PRR10 could acquire data at a maximum rate of around 10 kHz, only suitable for basic performance measurements. A new system with larger acceptance (30×30 cm^2), 48 scintillator slabs,[42] and a dedicated electronics capable to acquire data at a rate close to one MHz,[43] is in its completion phase.

Proton tomography systems have to handle large data rate and have to reconstruct images within minutes as required by the clinical utility. This is best achieved using graphics hardware boards (GPUs) that are the standard choice for most of the application described (e.g. see Ref. 44).

While very powerful, the pCT systems described so far are rather expensive and complex to operate. Promising results have been obtained with an intrinsically much simpler system using a stack of 40 nuclear emulsion plates interleaved with tissue equivalent absorbers to record the proton tracks emerging from a target;[45] tracks are reconstructed off-beam with very high accuracy using automated optical scanning. Unsuitable for real-time imaging, the system can be used for systematic investigations.

6. Concluding Remarks

With the continuous development of hadrontherapy worldwide, methods for improvement in quality assurance protocols have been developed to actively adjust the treatment plans with in-beam verifications of the patient position and anatomy. To this extent, proton beam tomography appears to be a promising tool, potentially providing in real-time the density map of the target, probed with the therapeutic beam itself, albeit at much reduced dose. Several setups have been developed and tested for this purpose, as described in this paper, together with methods for fast data retrieval and analysis. Further effort is required to both assess the valuableness of the method to achieve better treatment accuracy, and to improve the instrument design in view of a clinical use.

References

1. A. Tobias, *Cancer Res.* **18**, 121 (1958).
2. A. N. Smith, *Phys. Med. Biol.* **51**, R491 (2006).
3. U. Amaldi and G. Kraft, *J. Radiat. Res.* **48**, A27 (2007).
4. U. Amaldi and S. Braccini, *Eur. Phys. J. Plus* **126**, 70 (2011).
5. M. Jermann, *Int. J. Particle Ther.* **1**, 40 (2014).

6. ENVISION, http://envision.web.cern.ch/ENVISION/.
7. A. M. Koehler, *Science* **160**, 303 (1968).
8. NIST-PSTAR, http://www.physics.nist.gov./PhysRefData/Star/Text/PSTAR.html.
9. U. Schneider and E. Pedroni, *Med. Phys.* 353 (1995).
10. H. Bichsel, *Med. Phys.* **22**, 1721 (1995).
11. B. Schaffner and U. Pedroni, *Phys. Med. Biol.* **43**, 1579 (1998).
12. P. Zygmanski *et al.*, *Phys. Med. Biol.* **45**, 511 (2000).
13. U. Schneider *et al.*, *Med. Phys.* **32**, 195 (2005).
14. D. C. Williams, *Phys. Med. Biol.* **49**, 2899 (2004).
15. T. Satogata *et al.*, *IEEE Nucl. Sci. Symp. Conf. Rec.* **5**, 3667 (2005).
16. R. Schulte *et al.*, *Med. Phys.* **32**, 1035 (2005).
17. U. Schneider *et al.*, *Med. Phys.* **31**, 1046 (2004).
18. H. F.-W. Sadrozinski *et al.*, *IEEE Nucl. Sci. Symp. Conf. Rec.* **J2**, 4457 (2005).
19. S. N. Penfold *et al.*, *Med. Phys.* **37**, 5887 (2010).
20. J. Seco *et al.*, *Med. Phys.* **40**, 091717 (2012).
21. G. N. Ramanchandran and A. V. Lakshminarayanan, *Proc. Natl. Acad. Sci. USA* **68**, 2236 (1971).
22. L. A. Feldkamp *et al.*, *J. Opt. Soc. Am.* **A1**, 612 (1984).
23. S. N. Penfold *et al.*, *IEEE Nucl. Sci. Symp. Conf. Rec.* 4176 (2009).
24. E. Vanzi *et al.*, *Nucl. Instrum. Methods A* **730**, 184 (2013).
25. T. Li *et al.*, *Med. Phys.* **33**, 699 (2006).
26. R. Gordon *et al.*, *J. Theor. Biol.* **29**, 471 (1970).
27. D. C. Hansen *et al.*, *Med. Phys.* **41**, 031904-1 (2014).
28. K. M. Hanson *et al.*, *Phys. Med. Biol.* **26**, 965 (1981).
29. P. Pemler *et al.*, *Nucl. Instrum. Methods A* **432**, 483 (1999).
30. R. Schulte *et al.*, *IEEE Trans. Nucl. Sci.* **51**, 866 (2004).
31. H. F. Sadrozinski *et al.*, *IEEE Trans. Nucl. Sci.* **51**, 3 (2004).
32. T. Plautz *et al.*, Imaging *IEEE Trans. Med. Imaging* **33**, 875 (2014).
33. G. A. P. Cirrone *et al.*, *Nucl. Instrum. Methods A* **576**, 194 (2007).
34. V. Sipala *et al.*, *Nucl. Instrum. Methods A* **654**, 349 (2011).
35. C. Civinini *et al.*, *Nucl. Instrum. Methods A* **732**, 573 (2013).
36. C. Talamonti *et al.*, *Nucl. Instrum. Methods A* **612**, 571 (2010).
37. V. Sipala *et al.*, *Nucl. Instrum. Methods A* **658**, 171 (2011).
38. U. Amaldi *et al.*, *Nucl. Instrum. Methods A* **617**, 248 (2010).
39. F. Sauli, *Nucl. Instrum. Methods A* **386**, 531 (1997).
40. F. Sauli, *Comp. Biomed. Phys.* **8**, 367 (2014).
41. U. Amaldi *et al.*, *Nucl. Instrum. Methods A* **629**, 337 (1997).
42. M. Bucciantonio *et al.*, *Nucl. Instrum. Methods A* **732**, 564 (2013).
43. M. Bucciantonio *et al.*, *Nucl. Instrum. Methods A* **718**, 160 (2013).
44. K. Mueller *et al.*, *IEEE Nucl. Sci. Symp. Conf. Rec.* 3223 (2003).
45. S. Braccini *et al.*, *J. Instrum.* **5**, P09001 (2010).